NeuroImage 75 (2013) 204–212

Contents lists available at SciVerse ScienceDirect

NeuroImage

journal homepage: www.elsevier.com/locate/ynimg

A computational model for diffusion weighted imaging of myelinated white matter

Gregory T. Baxter [a], Lawrence R. Frank [a,b,*]

[a] Center for Scientific Computation in Imaging, Department of Radiology, University of California San Diego, 8950 Villa La Jolla Dr., Suite B227, La Jolla, CA 92037, USA
[b] Center for Functional MRI, Department of Radiology, University of California San Diego, 9500 Gilman Dr., #0677, La Jolla, CA 92093-0677, USA

ARTICLE INFO

Article history:
Accepted 25 February 2013
Available online 15 March 2013

Keywords:
Diffusion weighted imaging
Myelination
White matter
Monte Carlo simulation

ABSTRACT

The signal for diffusion weighted magnetic resonance imaging has previously been represented analytically and simulated numerically for a variety of model problems with idealized geometries. Numerical simulations hold the promise of computing the diffusion weighted MR signal for more complex realistic tissue architectures and physiological models. This paper investigates a white matter model consisting of a matrix of coated cylinders with distinct diffusion coefficients and spin concentrations for each of the cylinder core, the coating, and the surrounding bath and compares results with an the analytical solution developed by Sen and Basser for the long diffusion time limit.

Numerical simulations of diffusion weighted imaging experiments are performed for the three-medium model using a Monte Carlo diffusion simulation. Experiments are carried out for model parameters representing normal white matter. Pulse sequence parameters range from a low *b* value, long time limit, short pulse approximation to realistic clinical values.

For simulations in the short pulse width, long diffusion time limit, numerical simulations agree with the Sen–Basser analytical result. When tested with realistic pulse sequence parameters, numerical simulations show lower anisotropy than the analytical model predicts.

Published by Elsevier Inc.

Introduction

Diffusion-weighted MRI (DWI) provides a non-invasive imaging modality that offers the potential to probe tissue microstructure and physiology and thus provide important and unique information that informs a wide range of research and clinical applications. Its application to white matter is of particular interest because of its central role in neural connectivity and the devastating effects of the numerous degenerative white matter diseases. However, the signal attenuation caused by diffusion in the presence of magnetic field gradients provides information only about the aggregate diffusion within an imaging voxel. Unfortunately, the architectural and physiological complexity of intravoxel tissues precludes a simple relationship between the DWI signal and the underlying tissue structure and physiology. For example, diffusion anisotropy is typically used as a proxy for tissue integrity, but, in reality, inferring complex tissue characteristics from this quantity is severely ill-posed.

Analytical models for the signal attenuation have long been available for some simple geometries and idealized physiologies, such as impermeable boundaries, and these models have been useful analogs for biological structures, allowing some inferences about the structure and physiological state of the imaged tissue. But in order to obtain closed-form solutions, significant simplifications are typically employed. Analytical models generally leave out complicating details such as complex cellular structures and heterogeneous media, they frequently represent cell membranes as impermeable boundaries, and they often focus on simple pulse sequences. This disparity between simplified models and imaging situations and actual neural tissues in realistic DTI acquisitions makes inferences about tissue structure and integrity from real data problematic.

Numerical modeling offers an alternative, allowing more complex geometries, the inclusion of multiple tissue types and variable membrane permeability, and the specification of arbitrary pulse sequences in tractable ways. A versatile Monte Carlo based MR diffusion simulator (DiffSim) capable of modeling diffusion within arbitrary triangulated geometries and applying user-specified pulse sequence parameters has been demonstrated previously (Balls and Frank, 2009). Other packages are also available for diffusion-weighted MRI simulations. Hwang et al. (2003) developed a finite-difference method for simulating diffusion using histological images. They compared their results with known analytical solutions for impermeable cylinders. Camino (Cook et al., 2006; Hall and Alexander, 2009), like the approach in DiffSim, uses a Monte Carlo method to model diffusion. Differences between the DiffSim simulation environment and other options and the relative strengths of each approach have been discussed previously (Balls and Frank, 2009).

The critical importance of simulations becomes more evident as increasingly realistic representations of neural tissues are investigated. With the continuing development of more sensitive methods of DTI

* Corresponding author at: Center for Scientific Computation in Imaging, Department of Radiology, University of California San Diego, 8950 Villa La Jolla Dr., Suite B227, La Jolla, CA 92037, USA. Fax: +1 858 534 6322.
E-mail address: lfrank@ucsd.edu (L.R. Frank).

1053-8119/$ – see front matter. Published by Elsevier Inc.
http://dx.doi.org/10.1016/j.neuroimage.2013.02.076

data acquisitions and the broadening scope of their applicability to a wide range of basic science and important clinical applications, the ability to accurately infer quantitative information about tissue architecture, integrity, and connectivity from DTI should be enhanced. However, this goal is significantly hampered by the inability of simplistic analytical models to accurately parameterize complex neural tissues. One important application in which this issue arises is in the characterization of white matter changes—demyelination or other changes to white matter integrity—which play a central role in many degenerative disorders (Kraus et al., 2007; Kumra et al., 2004; Kutzelnigg et al., 2005; Madden et al., 2008; Phillips et al., 2001; Stricker et al., 2009). This is precisely the type of extension of an analytical model to a more realistic scenario where numerical simulations are essential.

In this paper, we are interested in extending the proposed analytical model of Sen and Basser (2005a,b), developed as an idealized, two-dimensional diffusion model in cylindrical coordinates, into a more realistic three-dimensional model of packed fibers within an actual DTI experiment. The Sen–Basser model describes diffusion in myelinated white matter consisting of an analytical solution for diffusion in an array of permeable, coated cylinders in the long-time limit. This model of multiple permeable media allows additional insight into the diffusion properties of white matter, and in particular the role of myelin, but its direct applicability to MR diffusion experiments with specific pulse sequence parameters remained an open question. Despite the potential importance of this model to the experimental investigation of white matter in both research and clinical applications, to our knowledge, there have been no experimental studies—physical or numerical—to determine how dependent their analytical model is on the assumption of a long diffusion time or how results might vary in research or clinical settings with realistic pulse sequences. One study did, however, examine some of the effects of geometry in this model (Davoodi-Bojd and Soltanian-Zadeh, 2011).

A critical step in investigating the efficacy of a model in providing useful information in DWI experiments is to quantitate the interplay of pulse sequence parameters and model parameters as they are ultimately manifest in the DWI signal. However, the Sen–Basser model depends only on properties of the material and not on pulse sequence parameters, and thus the study presented here required redeveloping the theory within the context of a DWI experiment, revealing the assumptions implicit in the original formulation, and then extending these results to realistic imaging scenarios.

This paper develops a numerical model of white matter DWI based upon the physical model described by Sen and Basser, consisting of a matrix of coated cylinders with distinct diffusion coefficients and spin concentrations for each of the cylinder core, the coating, and the surrounding bath. The primary significance of this work is our ability to quantitatively assess how numerous physical variables contribute to anisotropy in the DW signal, including packing density of the fibers and the thickness, diffusion coefficient, and water concentration of the myelin sheathing. In particular, two models of myelin changes are considered in more detail: thinner myelin sheathing and higher water concentration within the myelin.

Numerical simulation results are found to match the analytical solution given by Sen and Basser in the low b-value, short pulse width, long diffusion time limit. Using our extended theoretical analysis, the numerical simulations are then extended over more realistic imaging parameters, showing variation in the measured apparent diffusion as a function of changes to pulse sequence parameters. We find that of the two models we consider, changes to myelin water concentration have a greater effect on signal anisotropy than thinning myelin. We have thus developed a simulation environment capable of investigating the complex interplay of the DWI signal and myelination changes in a model white matter system capable of capturing some of the essential features of real white matter systems. This allows us to test how myelination changes associated with white matter diseases may manifest in DWI protocols.

Theory

A spin, j, diffusing in a time (t) dependent magnetic field gradient $\mathbf{G}(t)$ accrues a phase, θ_j generated by the spin's displacement in the direction of the magnetic field gradient

$$\theta_j(t) = \int_{t_0}^{t} \mathbf{G}(\tau)\cdot\mathbf{x}_j(\tau)d\tau. \tag{1}$$

where "·" represents the dot product. If time is discretized into N_t time steps of length dt, such that the gradient and the displacement are given at each time t_i, the integral can be approximated by a discrete sum:

$$\theta_j(t) = \sum_{i=0}^{N_t} \mathbf{G}(t_i)\cdot\mathbf{x}_j(t_i)dt. \tag{2}$$

For a collection of N_p diffusing spins, the complex signal attenuation is given by

$$E = \frac{1}{N_p}\sum_{j=1}^{N_p} e^{i\gamma\theta_j}. \tag{3}$$

where γ is the gyromagnetic ratio of water. The signal from a realistically sized voxel represented by Eq. (3) involves the sum over a tremendous number N_p of spins, the phases of which must all be tracked. The MCell Monte Carlo diffusion simulator (Stiles and Bartol, 2001) is a good match for this formulation of diffusion-weighted MR (Balls and Frank, 2009). MCell tracks each diffusing molecule, or spin, independently, making the sum in Eq. (3) straightforward. More importantly, MCell does not use a fixed diffusion step, but instead a random diffusion step chosen from a distribution matching the probability distribution for unbounded particles. As a result, an MR simulation based on MCell can respond accurately to diffusion-weighting gradient changes within a single time step, whereas fixed step length methods would require multiple time steps to produce accurate results. Thus short pulses can be more easily modeled, and longer pulses can potentially be modeled with many fewer time steps.

Diffusion fundamentals

Both the numerical simulation and the analytical model discussed here describe restricted diffusion, for which careful consideration of boundary conditions is critical. The problem formulation involves multiple diffusion coefficients and boundaries, but some details of the more basic problem—diffusion within a single medium with constant diffusion coefficient—need to be highlighted first because they are critical to the details of the numerical implementation. Fick's first law,

$$J(\mathbf{x},t) = -D\nabla C(\mathbf{x},t), \tag{4}$$

states that the flux of particles, J, is given as a function of the diffusion coefficient, D, and the gradient of the particle concentration, C. Adding a continuity equation,

$$\frac{\partial C(\mathbf{x},t)}{\partial t} + \nabla\cdot J(\mathbf{x},t) = 0, \tag{5}$$

which states that the change in concentration at a point is balanced by the gradient of the flux (and mass is conserved), we derive Fick's second law:

$$\frac{\partial C(\mathbf{x},t)}{\partial t} = -\nabla\cdot J(\mathbf{x},t) = \nabla\cdot D\nabla C(\mathbf{x},t). \tag{6}$$

When the diffusion coefficient is not a function of space, Eq. (6) can be written as

$$\frac{\partial C(\mathbf{x},t)}{\partial t} = D\nabla^2 C(\mathbf{x},t). \tag{7}$$

The Green's function, the response of this partial differential equation to an initial condition given as $\delta(\mathbf{x}-\mathbf{y})$ in an unbounded domain, is

$$G(\mathbf{x}-\mathbf{y},t) = \frac{1}{(4\pi Dt)^{n/2}} exp\left(\frac{-|\mathbf{x}-\mathbf{y}|^2}{4Dt}\right), \tag{8}$$

where n is the number of spatial dimensions.

The Green's function can also be viewed as the distribution of displacements from each spin's position at time $t = 0$ due to diffusion. In one dimension, the distribution of displacements is

$$G(x,t) = \frac{1}{\sqrt{4\pi Dt}} exp\left(-\frac{x^2}{4Dt}\right). \tag{9}$$

In the quasi-steady state case—when there is no concentration gradient—the net flux is zero, but there is still diffusion at the molecular level. The Green's function allows us to find the one-way flux across a plane within the quasi-steady state case. Since the Green's function represents the diffusion in an infinite space due to a point source (delta function), we can find, for some time τ, the number of spins diffused from the left past the origin since $t = 0$. In one dimension, the quantity diffused from points left of the origin ($x < 0$) past $x = 0$ by time τ is

$$Q_{\text{left}}(x,\tau) = C(x)\int_x^\infty G(y,\tau)dy = \frac{C(x)}{2}\left(1 + erf\left[\frac{x}{\sqrt{4D\tau}}\right]\right), \tag{10}$$

where $C(x)$ is the initial concentration at point x. Integrated over all space left of the origin, with a uniform concentration $C(x) = C_0$, the result simplifies to

$$\int_{-\infty}^0 Q_{\text{left}}(x,\tau)dx = C_0\sqrt{\frac{D\tau}{\pi}}. \tag{11}$$

This result is important in setting boundary conditions in a model with multiple media, as discussed below.

Modeling multiple media

Following Sen and Basser (2005a,b), we implement a three-medium model of coated cylinders. Each cylinder has a core (representing the axon) with a radius of r_c and a sheath (representing myelin) with an outer radius of r_s. These coated cylinders are arranged in a hexagonal array, with a spacing from center to center of L, as shown in Fig. 1. The packing density, f, of the array (the volume fraction of the coated cylinders) can be calculated from the geometry of the model: within the L by $L\sqrt{3}$ box of Fig. 1, the area occupied by coated cylinders is equal to the area of two circles of radius r_s. Thus f is given by

$$f = \frac{2\pi}{\sqrt{3}}\left(\frac{r_s}{L}\right)^2. \tag{12}$$

The three regions have distinct spin concentrations and diffusion coefficients. Inside the core, the spin concentration and diffusion coefficient are C_c and D_c, respectively. Similarly, the spin concentration and diffusion coefficient in the myelin sheath are C_s and D_s, while in the bath medium those quantities are C_b and D_b.

Media with different diffusion coefficients can be modeled by representing each diffusing spin as a distinct particle. A three-medium model requires three types of particles, each with its own diffusion coefficient, and with particles changing type at boundary transitions.

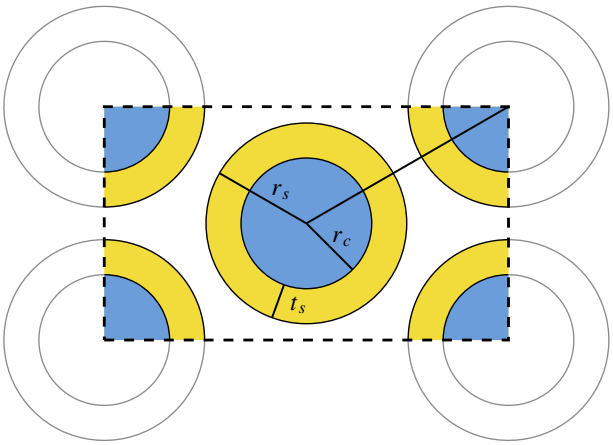

Fig. 1. The three medium model implemented in this study consists of coated cylinders with core (axon) radius r_c and sheath (myelin) outer radius r_s. The sheath thickness can be given as $t_s = r_s - r_c$. Cylinders are packed hexagonally with spacing (from center to center) L. The maximum value of r_s is $L/2$, at which point the array reaches its maximum packing density of about 0.907. The model is simulated within the bounding box indicated by dashed lines using periodic boundary conditions.

MCell sets the diffusion coefficient for each particle according to its molecule type, but boundary transition probabilities need to be adjusted to maintain quasi-steady-state spin concentrations.

The model implemented here, following the model described by Sen and Basser (2005a,b), includes no adjustable parameters for membrane permeability and introduces no boundary transition probability beyond what is required to maintain continuity and quasi-steady-state spin concentrations throughout the model. The constraints of continuity and quasi-steady-state-spin concentrations require the flux across medium boundaries to be the same in both directions. For two adjacent media, A and B, the flux from A to B must equal the flux from B to A. From Eq. (11) we know that fluxes at the boundary of each medium are proportional to $C_0\sqrt{D}$. The model allows the independent specification of spin concentration and diffusion coefficient in each medium, so the flux from A, $C_{0,A}\sqrt{D_A}$, generally does not equal the flux from B, $C_{0,B}\sqrt{D_B}$. In these cases, spins are allowed to migrate unimpeded from a low flux medium to a high flux medium: the probability of transition at the boundary is 1. Transitions from a high flux medium, A, to a low flux medium, B, are limited to occur at a probability

$$p_{AB} = \left(C_{0,B}\sqrt{D_B}\right)/\left(C_{0,A}\sqrt{D_A}\right), \tag{13}$$

defined such that the flux from the high flux medium ($p_{AB}C_{0,A}\sqrt{D_A}$) matches the flux from the low flux medium ($C_{0,B}\sqrt{D_B}$).

In one dimension, an estimate of the distribution due to diffusion in multiple media can be given by linear combinations of the Green's function (Eq. (8)). For the model evaluated here, the appropriate combination is based on the relative volume fractions and spin concentrations of the various media. The bath medium occupies a volume fraction of $1 - f$, the core medium occupies fr_c^2/r_s^2, and the sheath region occupies $f(1 - r_c^2/r_s^2)$. Using these volume fractions and the spin concentrations of each medium as the relative weights, we construct a volume-fraction-based distribution for the three media:

$$G_{\text{vf}}(x,t) = \sum_{i\in\{b,c,s\}} \frac{a_i C_i}{\sqrt{4\pi D_i t}} exp\left(-\frac{x^2}{4D_i t}\right) \tag{14}$$

where

$$\{a_b, a_c, a_s\} = \left\{(1-f), f\frac{r_c^2}{r_s^2}, f\left(1-\frac{r_c^2}{r_s^2}\right)\right\}. \tag{15}$$

This equation would hold exactly if all the media were aligned along the x-axis and isolated, with no transport of spins across boundaries.

Sen and Basser's analytical model

Sen and Basser note that in the long-time limit, the diffusion characteristics for the three-medium model described here, with cylinders of one medium coated with a second medium and arrayed in a third medium, are analogous to an electrostatics problem for coated cylinders. Nicorovici et al. (1993, 1995) found a solution for the effective dielectric constant of coated cylinders as a multipolar expansion. By a straightforward change of variables, setting = CD, Sen and Basser are able to use the results of Nicorovici et al. directly.

The product of the effective transverse diffusion coefficient, $D_{t,eff}$, and the effective spin concentration, C_{eff}, is then found in terms of the products of the spin concentration and diffusion coefficient in each region, i.e. $_c = C_{c0}D_c$, $_s = C_{s0}D_s$, and $_b = C_{b0}D_b$. The effective spin concentration is an average of the concentrations in the three media, weighted by the volume fractions of each medium:

$$C_{\text{eff}} = \sum_{i\in\{b,c,s\}} a_i C_{i0} \tag{16}$$

where a_i are given by Eq. (15). Truncating the multipole expansion to fourth order, Sen and Basser found the following result for diffusion transverse to an array of hexagonally packed cylinders:

$$D_{\text{t,eff}}C_{\text{eff}} = D_b C_b\left[1-2f\left(\gamma_1+f-\frac{0.07542f^6\gamma_7}{\gamma_5\gamma_7-1.06028f^{12}}\right)^{-1}\right]. \tag{17}$$

In this expression, γ_{2l-1} is a term Nicorovici et al. identified as the crucial quantity (the multipolar polarizability in their context of calculating effective dielectric constants for coated cylinders), defined as

$$\gamma_{2l-1} = \frac{(\epsilon_b-\epsilon_s)(\epsilon_s-\epsilon_c)r_c^{2(2l-1)} + (\epsilon_b+\epsilon_s)(\epsilon_s+\epsilon_c)r_s^{2(2l-1)}}{(\epsilon_b+\epsilon_s)(\epsilon_s-\epsilon_c)r_c^{2(2l-1)} + (\epsilon_b-\epsilon_s)(\epsilon_s+\epsilon_c)r_s^{2(2l-1)}}. \tag{18}$$

Sen and Basser represent the product of the effective longitudinal diffusion coefficient and the effective spin concentration as an average of the diffusion coefficients in the three media, weighted by the spin concentrations and volume fractions of each medium, i.e.

$$D_{\text{l,eff}}C_{\text{eff}} = \sum_{i\in\{b,c,s\}} a_i D_i C_{i0} \tag{19}$$

where a_i are given by Eq. (15). We note, however, that in the context of MR imaging, Eq. (19) does not hold exactly. $D_{\text{l,eff}}$ can be interpreted as the diffusion coefficient necessary to give the measured signal attenuation, according to

$$E_{\text{l}} = e^{-bD_{\text{l,eff}}}. \tag{20}$$

That is, given the longitudinal signal attenuation E_{l}, we calculate $D_{\text{l,eff}}$ as

$$D_{\text{l,eff}} = -ln(E_{\text{l}})/b. \tag{21}$$

In the case of three isolated media, with no spins crossing media boundaries, the signal attenuation responds according to

$$E_{\text{l}} = \sum_{i\in\{b,c,s\}} a_i C_{i0} e^{-bD_i} \tag{22}$$

so the effective longitudinal diffusion coefficient will be

$$D_{\text{l,eff}} = -\frac{1}{b}ln\left[\sum_{i\in\{b,c,s\}} a_i C_{i0} e^{-bD_i}\right]. \tag{23}$$

The various media spin concentrations here are relative concentrations, scaled such that $C_{\text{eff}} = 1$. An expansion of Eq. (23) around $b = 0$ gives Eq. (19) as the lowest order term. For clinically realistic b values (typically $b \approx 1000$ s/mm^2), the use of Eq. (19) is problematic, as we will show later.

Materials and methods

This work follows Sen and Basser, using the parameters they chose to represent normal white brain tissue: $D_b = 20\times10^{-4}$ mm^2/s, $D_c = 7.5\times10^{-4}$ mm^2/s, $D_s = 0.3\times10^{-4}$ mm^2/s, $C_{b0} = 0.95$, $C_{c0} = 0.88$, and $C_{s0} = 0.5$. Note that the concentrations given are not absolute, but are scaled to represent the relative concentrations in the various media. A base concentration of $C_0 = 100$ particles per μm^3 was used, so, $C_{b0} = 95$ μm^{-3}, $C_{c0} = 88$ μm^{-3}, and $C_{s0} = 50$ μm^{-3}. Based on these diffusion coefficients and concentrations and using Eq. (13), the transition probability of particle transitions from core to sheath was set at 0.114 and the probability of particle transitions from bath to sheath at 0.068. Note that all results below are for the general Sen–Basser model with permeable membranes, unless it is explicitly stated that impermeable membranes are being used (for comparison).

For the thickest sheaths simulated, the sheath spin concentration given by Sen and Basser results in a higher myelin water fraction (35%) than reported elsewhere (≈ 10–20%) (Lancaster et al., 2002; Whittall et al., 1997). Additional simulations were performed with $C_s = 0.15$, which corresponds to a myelin water fraction of 14% for a sheath thickness of 3.0 μm.

MCell models diffusion of particles interacting with surfaces represented by triangulated meshes. For this work, cylinders were modeled as extruded regular 64-gons. In order to compare our method with that of Sen and Basser, we use similar values of the core radius ($r_c = 6.0$ μm) along with a spacing between cylinders of $L = 18.2$ μm, allowing a maximum possible sheath radius $r_s = 9.1$ μm. The sheath thickness ($t_s = r_s - r_c$) varied from 0.2 μm to 3.0 μm. We note that these values reflect the abnormal state of cytotoxic edema (Sen and Basser, 2005a,b).

An infinite array was modeled by implementing a rectangular space (outlined with a dashed line in Fig. 1) with periodic boundary conditions. The dimensions of the simulated space were 18.2 μm by 32.5234 μm ($18.2\times\sqrt{3}$ Ëm) in the transverse plane, and 15.0 μm along the axis of the cylinders. A spin that hits a periodic boundary at position $\mathbf{r}$ is moved to the opposite boundary, and its original position, $\mathbf{r}_0$, is translated by the difference between boundaries so that the value of $\mathbf{r} - \mathbf{r}_0$ is continuous through boundary transitions. The purpose of the periodic boundary conditions is only to reduce the number of surfaces in the model: each particle still carries its absolute location, which is necessary for calculating phase shifts due to applied gradient fields.

For all simulations, a standard spin echo pulse sequence was used with bipolar diffusion weighting gradients represented by square pulses (no ramp time). The effects of diffusion through gradients other than the diffusion weighting gradients were not considered.

Results

Displacement distributions

It was expected that longitudinal spin displacement distributions given by numerical simulations would be similar to the isolated-media approximation given in Eq. (14), but significant differences between the longitudinal and transverse spin displacement distributions were expected. Diffusion simulations were performed for two different sheath thicknesses, 0.2 μm and 3.0 μm, near the minimum and maximum of the range of possible thicknesses, given the core radius of 6.0 μm and the spacing between cylinder centers of 18.2 μm. Histograms were generated of the spin displacements in the longitudinal and transverse (x and y, respectively) directions at three times, $t = 0.2\ r_c^2/D_c$, r_c^2/D_c, and $5.0\ r_c^2/D_c$. These results are shown in Fig. 2.

For the thin sheath, the isolated-media approximation of the displacement distribution appears very much like a standard Gaussian distribution, and the simulation results show only modest differences when comparing the transverse and longitudinal distributions. The transverse distribution is slightly narrower with a higher peak than the longitudinal distribution, and the longitudinal distribution is slightly broader with a lower peak than would be expected for isolated media.

For the thick sheath, the isolated-media approximation of the displacement distribution appears distinctly non-Gaussian, with much larger concentrations at very small displacements. This distribution results from the high volume fraction of the sheath medium, which has a much lower diffusion coefficient. Spins in the sheath medium move very little relative to spins in the core. These are the same effects seen for the thin sheath, with a slightly narrower, more peaked transverse distribution when compared with the longitudinal distribution, but these effects are especially pronounced at longer times. At the longest time ($t = 5.0\, r_c^2/D_c$), the peak concentration for the transverse displacement is more than twice the peak concentration for the longitudinal displacement. Thus, for the thick sheath, the apparent anisotropy grows with time.

Verification of the Sen–Basser theory in the low *b* value, narrow pulse, long diffusion time limit

The time regimes under which the original Sen–Basser analytical approach is valid are somewhat restrictive. Since they avoided any interaction with a pulse sequence, numerical simulations would be expected to agree most closely to their results when the narrow pulse approximation is valid, i.e. the pulse width, δ, is much less than the diffusion time $\tau = \Delta - \delta/3$, because this approximation disregards effects due to finite pulse gradient widths. Furthermore, the analytical estimate for the transverse diffusion coefficient (Eq. (17)) was derived in the long-time limit. In addition, their formulation

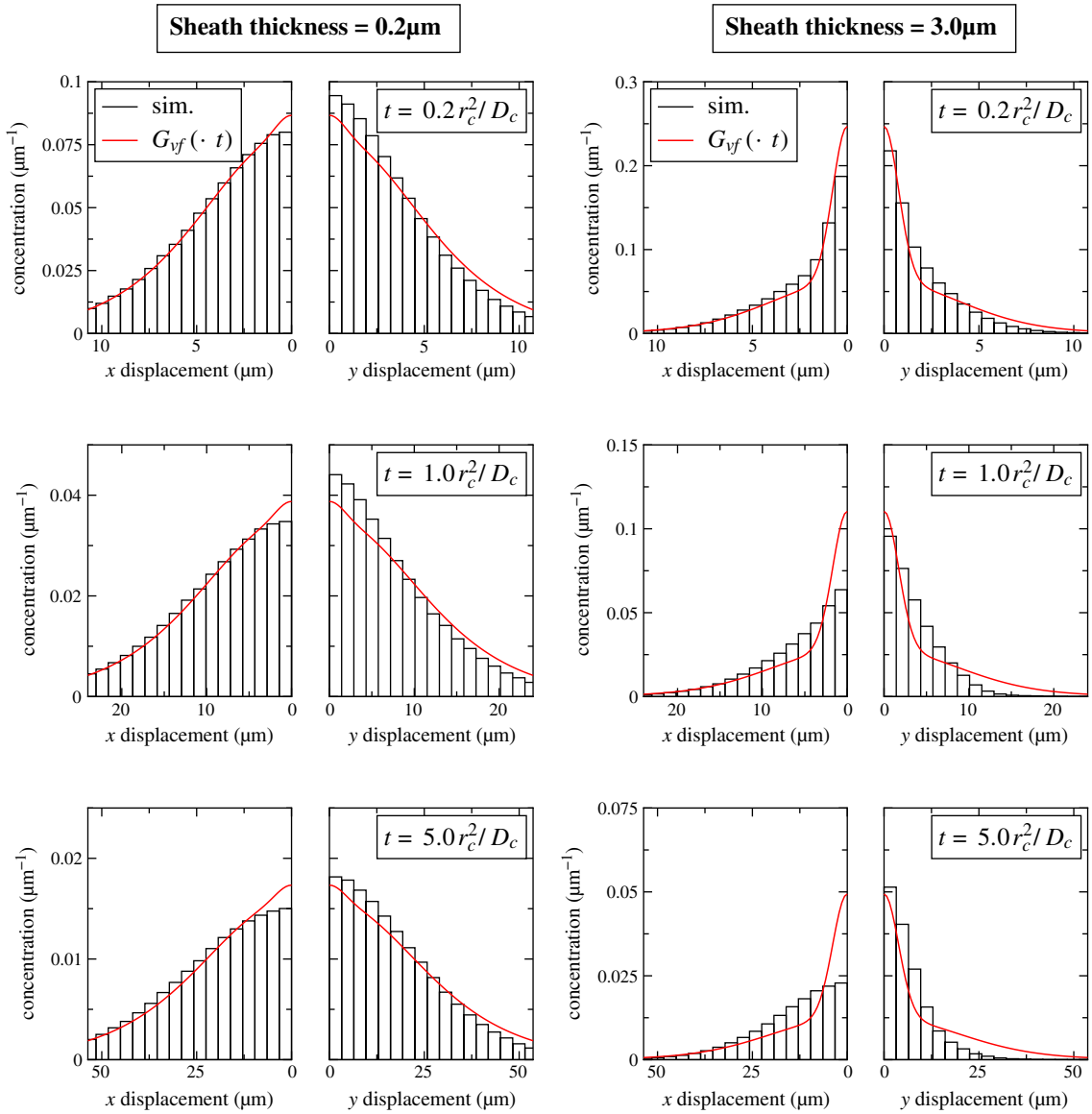

Fig. 2. Spin displacement distributions given by numerical simulation are shown as histograms, while the distributions predicted by the isolated-media estimate of Eq. (14) are indicated by the red line. For thin sheathing (left), the effects of the sheath are small, and the distribution appears similar to a standard Gaussian distribution. The simulations show little difference between the longitudinal (x) and transverse (y) distributions. For thick sheaths (right), the effect of the sheathing is much more pronounced, even in the isolated-media estimate.

employs a low-order estimate of the longitudinal diffusion coefficient (Eq. (19)) which will be most accurate for small b values, but becomes increasingly problematic for higher b values. Nevertheless, these represent important limiting cases, and are just as easily simulated in order to confirm (or not) the validity of their formulation.

As expected, with a b value of $0.01/D_c$, τ of 5 times r_c^2/D_c, and δ of $\tau/1200$ very good agreement is found between numerical simulations and the Sen–Basser model. The longitudinal apparent diffusion coefficient, $D_{l,eff}$, was within 1% of the value predicted by Eq. (19) over the entire range of sheath thicknesses. The transverse ADC, $D_{t,eff}$, showed more variation, deviating from Eq. (17) by 12% for the thickest sheaths. For sheaths less than 2.5 μm thick, the results agreed to within 5%. These results can be seen in Fig. 3.

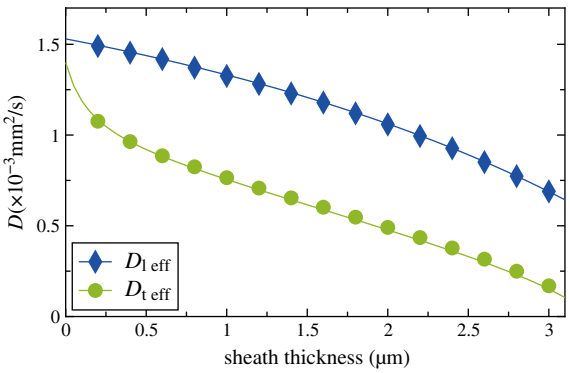

Fig. 3. The effective longitudinal ADC, $D_{l,eff}$, and the effective transverse ADC, $D_{t,eff}$, calculated from simulations both agree well with the analytical models for a small b value ($b = 0.01/D_c$), a long diffusion time ($\tau = 5\ r_c^2/D_c$), and a narrow pulse ($\delta = \tau/1200$). Results from simulations are shown with symbols, and analytical models are shown with lines.

Variations in longitudinal diffusion coefficient with increasing *b* values

Application of the model to human DWI experiments requires adapting the model to be valid for larger b values as Eq. (19) becomes less accurate at predicting the longitudinal diffusion coefficient. We proposed another formulation in Eq. (23), which holds independent of b value for isolated media. This result was first verified for isolated media by running simulations with impermeable boundaries between media. The b values were varied over a range of values, scaled as a/D_c, with $a = [0.01,0.1,1.0]$, resulting in b values of 13.33, 133.3, and 1333 s/mm^2. While maintaining the long diffusion time and the narrow pulse, with τ constant at 5 times r_c^2/D_c and δ constant at $\tau/1200$, the b values were adjusted by varying the gradient strength. At the largest b value simulated, the calculated longitudinal ADC, $D_{l,eff}$, was significantly reduced, but in all cases the results agreed well with the extended expression for $D_{l,eff}$ given in Eq. (23), as seen in Fig. 4.

When boundaries between media are made fully permeable, the results fall between the predictions of Eqs. (19) and (23). The deviations between the results from simulation and s 19 and are smaller, but still significant at the largest b value, as seen in Fig. 4. It is interesting to note that for permeable boundaries the exchange between compartments results in an increase in the longitudinal diffusion coefficient relative to the case of impermeable boundaries, as seen in Fig. 4. While this is clearly evident in the simulations, the analytical model is incapable of explaining this effect and can only produce the limiting ranges expressed by Eqs. (19) and (23).

Variations in transverse diffusion coefficient with changing *b* values, diffusion times, and pulse widths

An extended analytical model for the transverse diffusion coefficient has not been developed here, but in simulation results significant effects were observed when simulations vary from the small b value, long diffusion time limit of the original Sen–Basser formulation. A known confound in the analysis of clinical DWI experiments is the influence of the finite width of the diffusion weighting gradients. Yeh et al. (2010) recently examined these effects through both numerical simulations and physical experiments of DWI of impermeable cylinders. They examined the effects of varying pulse widths, and presented their results as graphs of signal vs. gradient direction (angle). Their results agreed well with analytical solutions for cylinders, such as the matrix formalism given by Grebenkov (2007). DiffSim likewise produces results consistent with the analytical solution for impermeable cylinders (see Fig. 5).

In order to isolate the combined influence of larger diffusion sensitivity through increased b value and diffusion times τ, b was varied from $0.01/D_c$ to $1/D_c$ and τ was varied from 0.2 to 5 times r_c^2/D_c, but τ/δ was kept constant at 1200 so that simulations remained in the range of the narrow pulse approximation to mitigate confounding effects due to finite pulse widths (Yeh et al., 2010). At low b values, deviating from the long diffusion time limit results in larger diffusion coefficients than predicted by Eq. (17), with the difference being more pronounced as the sheath thickness grows. At the largest b value simulated ($b = 1333$ s/mm^2), it was found that the calculated $D_{t,eff}$ was lower than predicted by Eq. (17) for thin sheaths, but higher (especially for short τ) for thick sheaths. For the largest b value, the results did not converge to the analytical model even at the longest τ simulated. These results can be seen in Fig. 6.

For completeness, the effects of varying the pulse width were then included, and found to be much less pronounced than the effects of varying either the b value or the diffusion time. Increasing pulse width reduces the apparent transverse diffusion coefficient, but at long diffusion times the differences are very small. The effects of varying pulse widths are shown in Fig. 6.

Short diffusion times significantly affect the ratio of $D_{l,eff}/D_{t,eff}$, which can be viewed as a measure of anisotropy. The analytical model given by Sen and Basser predicts that anisotropy grows gradually as sheath thickness increases but begins to grow much more rapidly for sheath thicknesses greater than about 2.5 μm as the bath region becomes increasingly restricted. In numerical simulations the anisotropy curve is greatly flattened when τ is short, as shown in Fig. 7.

Signal as a function of gradient angle for clinically realistic pulse sequence parameters

Up to this point, we have considered independently varied pulse sequence parameters over a wide range of values. In clinical experiments, however, the pulse sequence parameters are rarely chosen independently. In order to reduce scan time and cost, scans are typically performed with gradients set to the maximum possible for the scanner, the time between pulses minimized, and the pulse width long enough to produce the desired b value. To assess the model under more clinically realistic conditions, a set of simulations with clinically realistic pulse sequence parameters was performed by setting the time between pulses, $\Delta - \delta$, to 3 ms and the gradient strength to 4.0 G/cm, and varying δ to achieve b values of 1000, 4000, and 8000 s/mm^2.

The three-medium simulations were repeated for two sheath thicknesses: an intermediate thickness (1.6 μm) which is approximately half the maximum possible thickness, and a near-maximal thickness (3.0 μm). The simulations were also repeated for two sheath spin concentrations: a high concentration (0.5, used by Sen and Basser) and a lower concentration (0.15) which, for the thickest sheath, better matches the normal myelin water fraction given elsewhere (Lancaster et al., 2002; Whittall et al., 1997).

Signal for the low spin concentration, thick myelin sheath model takes on the familiar “peanut” shape (Fig. 8a), similar to the signal

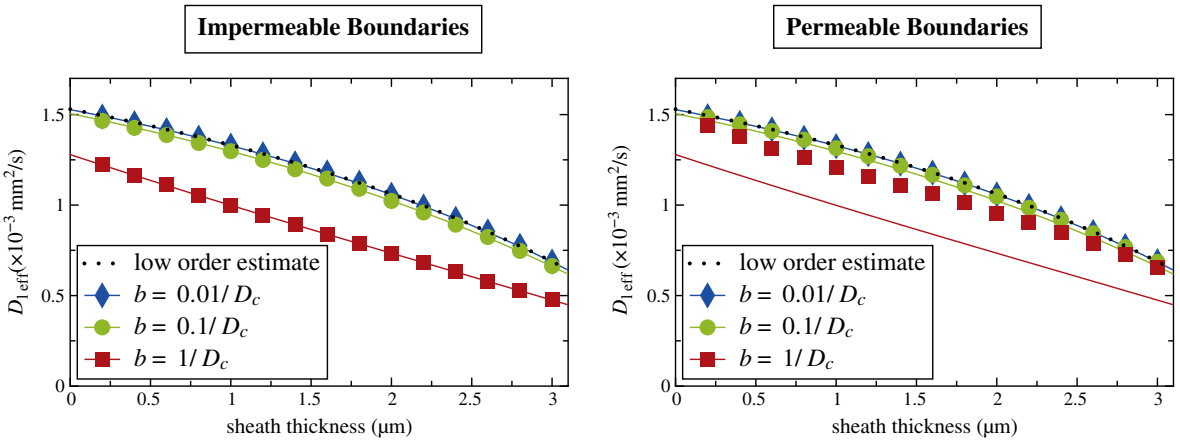

Fig. 4. For simulations with impermeable boundaries (left), the effective longitudinal ADC, $D_{l,eff}$, calculated from simulations (symbols) agrees well with the extended analytical expression for isolated media given in Eq. (23) (lines), with $D_{l,eff}$ reduced for larger b values. For simulations with permeable boundaries (right), the effective longitudinal ADC, $D_{l,eff}$, (symbols) falls between the values predicted by Eq. (19) (dotted line) and Eq. (23) (solid colored lines). $D_{l,eff}$ is reduced for larger b values, but the effect is not as great as when boundaries between media are impermeable.

generated for the idealized impermeable cylinder model (Fig. 5). The model with low spin concentration in a thinner myelin sheath (Fig. 8b) shows similar anisotropy: $D_{l,eff}/D_{t,eff} = 3.6$ for the thinner myelin model at a b value of 8000 s/mm^2, slightly greater than for the thick myelin model's anisotropy of 3.2. The most visible difference between the results for the two models is the reduced signal for the thinner myelin model, corresponding to a higher mean diffusivity. This is a result of averaging over a volume that contains a larger volume fraction of spins outside the myelin whose diffusion coefficients are larger. The model with higher spin concentration in a thick myelin sheath results in significantly reduced anisotropy (Fig. 8c). $D_{l,eff}/D_{t,eff}$ falls to 2.1 as more signal is retained in the longitudinal direction because of the greater density of spins with a low diffusion coefficient in the myelin sheath. The increased spin density in the myelin sheath also leads to a slightly lower mean diffusivity.

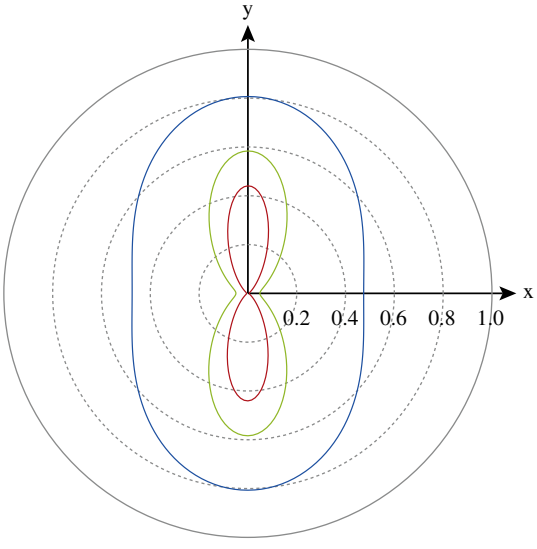

Fig. 5. In a simulation of an isolated cylinder of a single medium with $D = 7.5 \times 10^{-4}$ mm^2/s (the value of D_c used in other simulations) and finite-width gradient pulses, results from DiffSim show the standard "peanut" shape for the signal. For these simulations, $G = 4.0$ G/cm and $\Delta - \delta = 3$ ms. Pulse widths were selected to produce three different b values: $b = 1000$ s/mm^2, with $\delta = 22.2$ ms (outermost line, shown in blue); $b = 4000$ s/mm^2, with $\delta = 36.0$ ms (intermediate line, shown in green); and $b = 8000$ s/mm^2, with $\delta = 45.7$ ms (innermost line, shown in red). The cylinders are oriented parallel to the x axis.

Discussion

The combination of multiple media with differing diffusion characteristics within a single imaging voxel leads to non-Gaussian diffusion behavior. These differences arise even when the media are isolated from one another. The non-Gaussian diffusion behavior is predicted by the analytical model for the effective longitudinal diffusion coefficient, $D_{l,eff}$ (Eq. (23)). As a result of this non-Gaussian diffusion, the effective diffusion coefficient varies as a function of the b value, as can be seen in simulated results (Fig. 4).

The transverse effective diffusion coefficient, $D_{t,eff}$, and the anisotropy, $D_{l,eff}/D_{t,eff}$, are quite sensitive to pulse sequence parameters. Numerical simulations reproduce the results given by Sen and Basser only for experiments at very low b values and fairly long values of τ. Differences are most pronounced at high b values, such that the dependence of $D_{t,eff}$ and especially anisotropy on sheath thickness is greatly reduced or eliminated entirely.

We note that significant differences appear between the analytical formulation given by Sen and Basser and results from numerical simulations at a b value of only 1333 s/mm^2. As a result, using the analytical formulation to predict precise values for apparent diffusion coefficients or anisotropy may be inappropriate for many clinically relevant pulse sequences. The largest differences occur for short τ, but the shortest values simulated, $\tau = 0.2\ r_c^2/D_c$ and $\tau = 1.0\ r_c^2/D_c$, are 9.6 ms and 48 ms, respectively. These values are within the range commonly seen in clinical applications, whereas the longest τ, 5.0 r_c^2/D_c or 240 ms, is longer than would generally be used. For small bore, high field systems where very large b values and short τ's are attainable, these effects will become more pronounced.

The weak relationship between sheath thickness and anisotropy seen in Fig. 7, most especially at shorter τ, was unexpected. Plots of signal vs. gradient angle (Fig. 8) highlighted this effect for models with a high spin concentration in the myelin sheath. Simulations with a lower spin concentration in the myelin sheath—matching myelin water fraction values for normal adults (Lancaster et al., 2002; Whittall et al., 1997)—produced results with greater anisotropy, even for thinner myelin sheaths.

A parameterized model capable of predicting the influences of physiological and architectural parameters on the DWI signal from myelinated white matter opens up the possibility of developing and testing

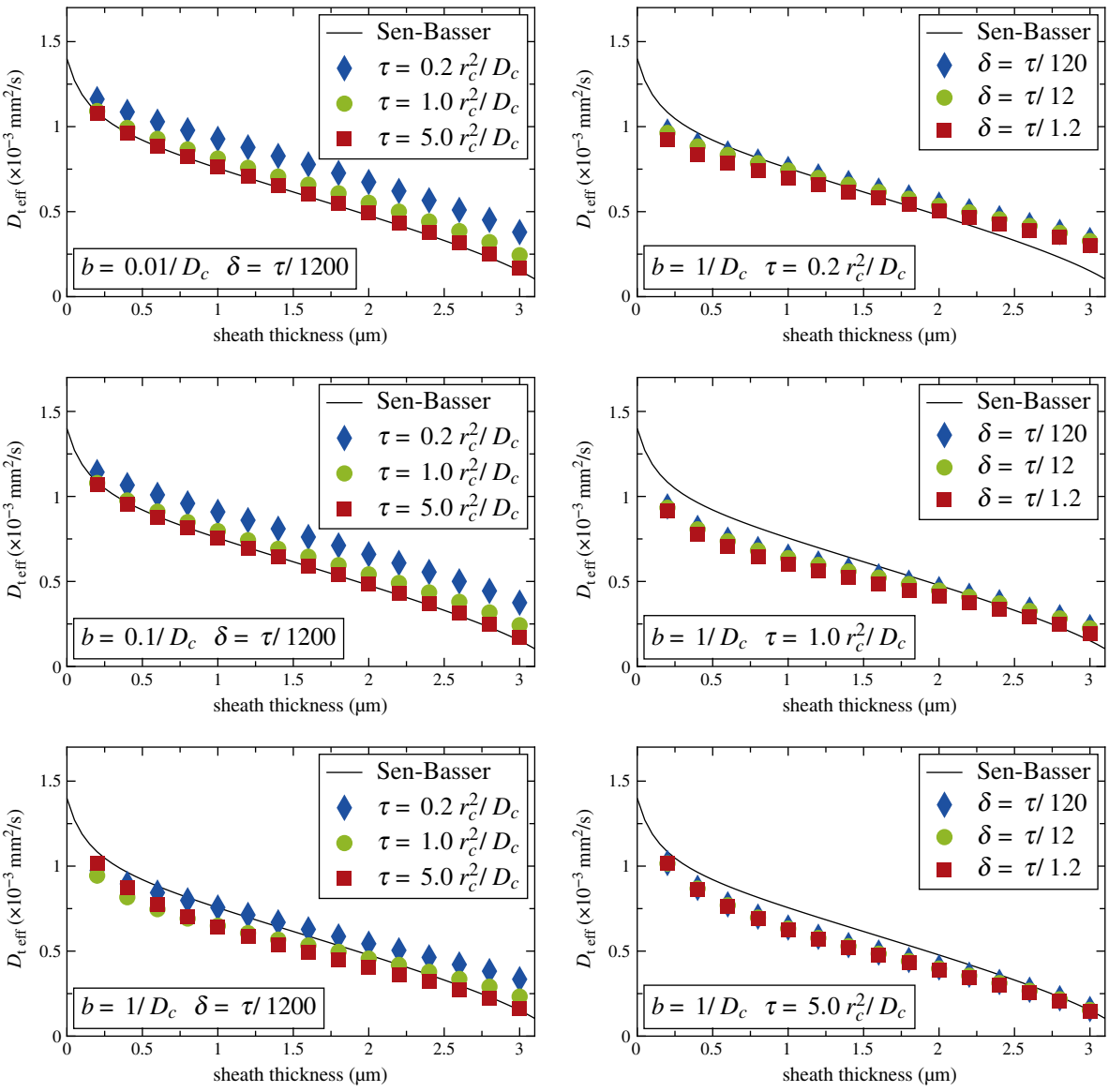

Fig. 6. The effective transverse ADC, $D_{t,eff}$, calculated from simulations agrees well with the analytical model given by Sen and Basser for long values of diffusion time, τ, and small b values (red squares, upper left graph). For short pulse widths (graphs at left) and shorter values of τ, the calculated $D_{t,eff}$ is generally larger than predicted by the Sen–Basser model, especially as the sheath thickness grows. Variations in the pulse width, δ, (graphs at right) have a relatively smaller effect than changes in τ.

quantitative clinical metrics for white matter disorders. Models described here focused on two possible changes to myelinated white matter: a reduction in myelin thickness and an increase in myelin water concentration. Thinning myelin did not reduce anisotropy but did result in greater mean diffusivity. An increase in myelin water concentration decreased anisotropy significantly, even without a change in myelin thickness. Recent clinical research (Laule et al., 2008; Sirrs et al., 2007) involving T_2 relaxation measurements has demonstrated that, at least in multiple sclerosis and phenylketonuria, myelin water concentration is unchanged by disease processes and that myelin water fraction changes can be attributed to changes in myelination. Numerical simulations of T_2 relaxation would be an important adjunct to the current research. While the goal of validation and extension of the Sen–Basser model in this paper required the use of the physical dimensions used in their work (Sen and Basser, 2005a,b) based on cytotoxic edema, our future work will involve the application of this simulation model to a wide variety of both normal and pathological conditions.

Though we recognize that this model is ultimately a significantly simplified model of true myelinated white matter, the computational

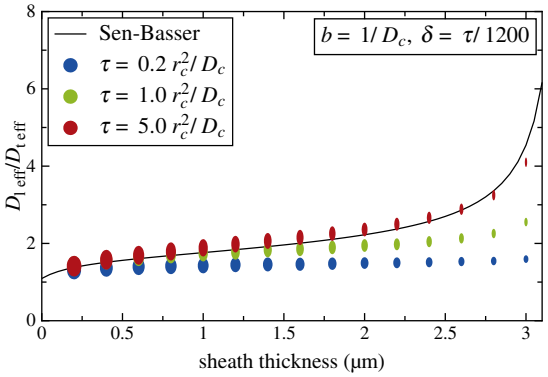

Fig. 7. For short τ, the measured anisotropy ($D_{l,eff}/D_{t,eff}$) is much more weakly affected by changes in sheath thickness. For longer τ simulated results approach the analytical model given by Sen and Basser. The plot points are the standard (2D) diffusion ellipsoids with major and minor eigenvalues, $D_{l,eff}$ and $D_{t,eff}$, shown as the vertical and horizontal axes.

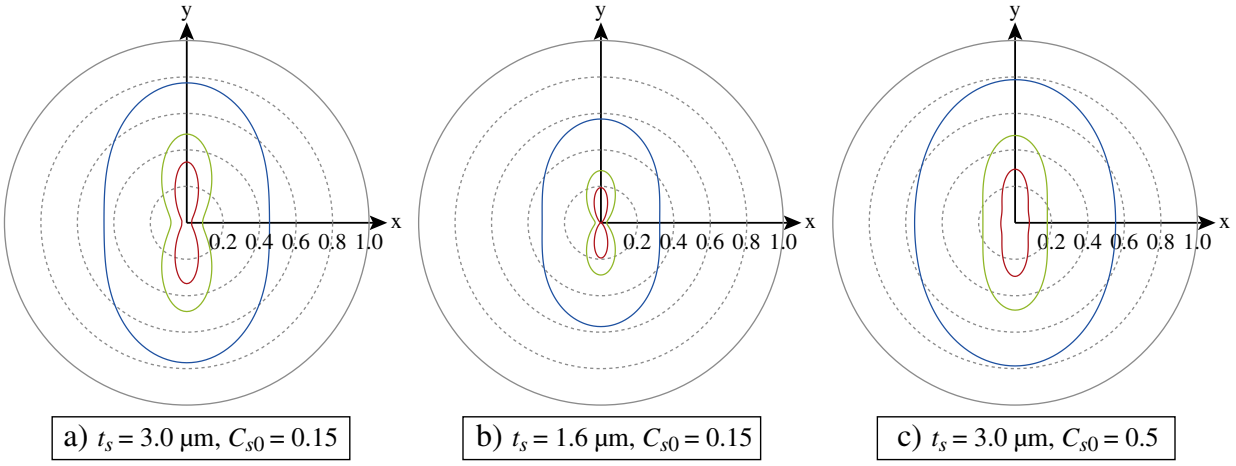

Fig. 8. Signal vs. gradient angle for the three-medium model with $D_b = 20 \times 10^{-4}$ mm^2/s, $D_c = 7.5 \times 10^{-4}$ mm^2/s, $D_s = 0.3 \times 10^{-4}$ mm^2/s, $C_{b0} = 0.95$ and $C_{c0} = 0.88$. For all simulations $G = 4.0$ G/cm and $\Delta - \delta = 3.0$ ms. As in the isolated cylinder simulations shown in Fig. 5, these simulations were performed at three b values: $b = 1000$ s/mm^2 ($\delta = 22.2$ ms, outermost line, shown in blue); $b = 4000$ s/mm^2 ($\delta = 36.0$ ms, intermediate line, shown in green); and $b = 8000$ s/mm^2 ($\delta = 45.7$ ms, innermost line, shown in red). The cylinders are oriented parallel to the x axis. a) Simulation with $t_s = 3.0$ μm and $C_{s0} = 0.15$: the signal takes on a "peanut" shape at high b values. b) Simulation with $t_s = 1.6$ μm and $C_{s0} = 0.15$: reduced myelin thickness does not significantly change the shape of the signal, but noticeably reduces its magnitude. c) Simulation with $t_s = 3.0$ μm and $C_{s0} = 0.5$: increased spin density in the myelin sheath (increased myelin water concentration) greatly reduces the anisotropy as more signal is retained in the longitudinal direction.

platform is flexible enough to incorporate a wide range of more complex refinements. Moreover, numerical simulations could be used to test further clinical hypotheses in situations where analytical formulations are not available.

Conclusion

A theoretical and numerical investigation of a myelinated axon model was developed based upon the analytical three-medium model described by Sen and Basser. The ability to test a wide range of effects relatively quickly and inexpensively makes numerical simulation a useful adjunct to theory and physical experiments. By simulating diffusion MRI experiments on this model we were able to confirm their theoretical results in the long diffusion time limit and to investigate the effects of more clinically relevant parameters involving shorter diffusion times and other variations in pulse sequence parameters. The simulations highlight deviations from the analytical model for realistic pulse sequence parameters. Specifically, measured anisotropy may be significantly reduced from the value predicted by the long diffusion time analytical model. Further, our numerical experiments demonstrated greater changes in anisotropy due to changes in myelin water concentration than due to changes in sheath thickness. The ability to investigate quantitative relationships between parameterized models of myelinated axons and the resultant DWI signals opens the possibility of using DWI to derive clinically relevant metrics for white matter diseases.

Conflict of interest statement

There is no conflict of interest.

Acknowledgments

The authors are grateful to Peter Basser for his encouragement of this research. This work was supported by NIH grant R01 MH096100 and by NSF grants PHY-1201238 and EF-0850369.

References

Balls, G., Frank, L., 2009. A simulation environment for diffusion weighted MR experiments in complex media. Magn. Reson. Med. 62, 771–778.
Cook, P., Bai, Y., Nedjati-Gilani, S., Seunarine, K., Hall, M., Parker, G., Alexander, D., 2006. Camino: open-source diffusion-MRI reconstruction and processing. Proceedings of the 14th Annual Meeting of ISMRM, Seattle, WA, p. 2759.
Davoodi-Bojd, E., Soltanian-Zadeh, H., 2011. Evaluation of diffusion models of fiber tracts using diffusion tensor magnetic resonance imaging. Magn. Reson. Imaging 29, 1175–1185.
Grebenkov, D., 2007. NMR survey of reflected Brownian motion. Rev. Mod. Phys. 79, 1077–1137.
Hall, M., Alexander, D., 2009. Convergence and parameter choice for Monte-Carlo simulations of diffusion MRI. IEEE Trans. Med. Imaging 28, 1354–1364.
Hwang, S., Chin, C., Wehrli, F., Hackney, D., 2003. An image-based finite difference model for simulating restricted diffusion. Magn. Reson. Med. 50, 373–382.
Kraus, M.F., Susmaras, T., Caughlin, B.P., Walker, C.J., Sweeney, J.A., Little, D.M., 2007. White matter integrity and cognition in chronic traumatic brain injury: a diffusion tensor imaging study. Brain 130, 2508–2519.
Kumra, S., Ashtari, M., McMeniman, M., Vogel, J., Augustin, R., Becker, D.E., Nakayama, E., Gyato, K., Kane, J.M., Lim, K., Szeszko, P., 2004. Reduced frontal white matter integrity in early-onset schizophrenia: a preliminary study. Biol. Psychiatry 55, 1138–1145.
Kutzelnigg, A., Lucchinetti, C.F., Stadelmann, C., Brck, W., Rauschka, H., Bergmann, M., Schmidbauer, M., Parisi, J.E., Lassmann, H., 2005. Cortical demyelination and diffuse white matter injury in multiple sclerosis. Brain 128, 2705–2712.
Lancaster, J.L., Andrews, T., Hardies, L.J., Dodd, S., Fox, P.T., 2002. Three-pool model of white matter. J. Magn. Reson. Imaging 17, 1–10.
Laule, C., Kozlowski, P., Leung, E., Li, D.K., MacKay, A.L., Moore, G.W., 2008. Myelin water imaging of multiple sclerosis at 7 T: correlations with histopathology. Neuroimage 40, 1575–1580.
Madden, D.J., Spaniol, J., Costello, M.C., Bucur, B., White, L.E., Cabeza, R., Davis, S.W., Dennis, N.A., Provenzale, J.M., Huettel, S.A., 2008. Cerebral white matter integrity mediates adult age differences in cognitive performance. J. Cogn. Neurosci. 21, 289–302.
Nicorovici, N., McPhedran, R., Milton, G., 1993. Transport properties of a three-phase composite material: the square array of coated cylinders. Proc. R. Soc. Lond. A Math. Phys. Sci. 442, 599–620.
Nicorovici, N., McKenzie, D., McPhedran, R., 1995. Optical resonances of three-phase composites and anomalies in transmission. Opt. Commun. 117, 151–169.
Phillips, M.D., McGraw, P., Lowe, M.J., Mathews, V.P., Hainline, B.E., 2001. Diffusion-weighted imaging of white matter abnormalities in patients with phenylketonuria. Am. J. Neuroradiol. 22, 1583–1586.
Sen, P., Basser, P., 2005a. A model for diffusion in white matter in the brain. Biophys. J. 89, 2927–2938.
Sen, P., Basser, P., 2005b. Modeling diffusion in white matter in the brain: a composite porous medium. Magn. Reson. Imaging 23, 215–220.
Sirrs, S.M., Laule, C., Mädler, B., Brief, E.E., Tahir, S.A., Bishop, C., MacKay, A.L., 2007. Normal-appearing white matter in patients with phenylketonuria: water content, myelin water fraction, and metabolite concentrations. Radiology 242, 236–243.
Stiles, J., Bartol, T., 2001. Monte Carlo methods for simulating realistic synaptic microphysiology using MCell. In: De Schutter, E. (Ed.), Computational Neuroscience: Realistic Modeling for Experimentalists. CRC Press, Boca Raton, FL, pp. 87–127.
Stricker, N., Schweinsburg, B., Delano-Wood, L., Wierenga, C., Bangen, K., Haaland, K., Frank, L., Salmon, D., Bondi, M., 2009. Decreased white matter integrity in late-myelinating fiber pathways in Alzheimer's disease supports retrogenesis. Neuroimage 45, 10–16.
Whittall, K.P., Mackay, A.L., Graeb, D.A., Nugent, R.A., Li, D.K.B., Paty, D.W., 1997. In vivo measurement of T2 distributions and water contents in normal human brain. Magn. Reson. Med. 37, 34–43.
Yeh, C., Tournier, J., Cho, K., Lin, C., Calamante, F., 2010. The effect of finite diffusion gradient pulse duration on fibre orientation estimation in diffusion MRI. Neuroimage 51, 743–751.